JACS
JOURNAL OF THE AMERICAN CHEMICAL SOCIETY
Article
Cite This: J. Am. Chem. Soc. 2018, 140, 814−826
pubs.acs.org/JACS

Singlet Fission Involves an Interplay between Energetic Driving Force and Electronic Coupling in Perylenediimide Films

Aaron K. Le,[§,†] Jon A. Bender,[§,†] Dylan H. Arias,[‡] Daniel E. Cotton,[†] Justin C. Johnson,[‡] and Sean T. Roberts*[,†]

[†]Department of Chemistry, The University of Texas at Austin, Austin, Texas 78712-1224, United States
[‡]National Renewable Energy Laboratory, Golden, Colorado 80401-3305, United States

Supporting Information

ABSTRACT: Due to its ability to offset thermalization losses in photoharvesting systems, singlet fission has become a topic of research interest. During singlet fission, a high energy spin-singlet state in an organic semiconductor divides its energy to form two lower energy spin-triplet excitations on neighboring chromophores. While key insights into mechanisms leading to singlet fission have been gained recently, developing photostable compounds that undergo quantitative singlet fission remains a key challenge. In this report, we explore triplet exciton production via singlet fission in films of perylenediimides, a class of compounds with a long history of use as industrial dyes and pigments due to their photostability. As singlet fission necessitates electron transfer between neighboring molecules, its rate and yield depend sensitively on their local arrangement. By adding different functional groups at their imide positions, we control how perylenediimides pack in the solid state. We find inducing a long axis displacement of ∼3 Å between neighboring perylenediimides gives a maximal triplet production yield of 178% with a fission rate of ∼245 ps despite the presence of an activation barrier of ∼190 meV. These findings disagree with Marcus theory predictions for the optimal perylenediimide geometry for singlet fission, but do agree with Redfield theory calculations that allow singlet fission to occur via a charge transfer-mediated superexchange mechanism. Unfortunately, triplets produced by singlet fission are found to decay over tens of nanoseconds. Our results highlight that singlet fission materials must be designed to not only produce triplet excitons but to also facilitate their extraction.

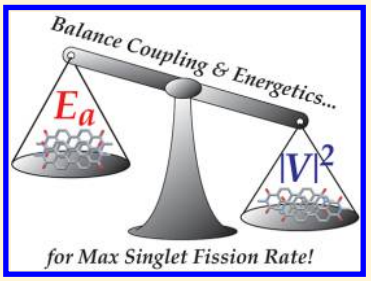

1. INTRODUCTION

Singlet fission (SF) is a process that occurs in select organic materials wherein a spin-singlet exciton divides its energy among two neighboring molecules to form a pair of spin-correlated spin-triplet excitons.[1,2] First observed in anthracene crystals half a century ago,[3] SF has experienced renewed interest due to its potential to enhance light harvesting schemes by producing multiple excited electrons from a single photon absorption event. Importantly, SF materials can mitigate thermalization losses in photovoltaic cells. Semiconductors that absorb photons with energy exceeding their bandgap typically dissipate this extra energy as heat.[4] A SF material placed in series with a semiconductor solar cell can instead absorb high energy photons and produce pairs of excitons that can each be passed to the underlying cell, reducing energy lost to heat and leading to as much as a 40% improvement of the cell's efficiency.[5−7] SF materials also have potential utility in photocatalytic schemes requiring multiple electron injection,[5] and may play a role as photoprotectants in biological systems by rapidly dissipating high energy photoexcitations.[8,9] In addition, SF's inverse, triplet fusion, can be used to produce fluorescent light emitting diodes[10] and material composites that upconvert incoherent infrared radiation into the visible spectral range[11−15] for both photovoltaic and sensing applications.

Designing SF materials suitable for the applications above remains challenging as they must simultaneously satisfy multiple criteria. For light harvesting applications in particular, a SF material must meet the energetic requirement that the energy of its lowest spin-triplet state be half that of its lowest spin-singlet state, $E(S_1) = 2E(T_1)$, while also possessing a high degree of photostability and a large molar extinction coefficient. Additionally, triplet excitons should be sufficiently energetic to sensitize charge carrier production in a complementary semiconductor. While SF has been reported in carotenoids,[8,9] benzofurans,[16,17] diketopyrrolopyrroles,[18] and conjugated polymers,[19−21] much of our understanding of this process remains shaped by experiments and calculations performed on the family of acenes. To some extent, the large focus placed on acenes such as tetracene and pentacene is historical; SF was first discovered in anthracene crystals[3] and soon after reported in crystalline tetracene.[22−24] These materials have remained in the spotlight as a result of their high SF yields in molecular crystals,[25−28] thin films,[29−31] and covalently tethered dimers,[32−36] oligomers,[37] and polymers.[38] However, despite high triplet yields, designing light harvesting applications that incorporate acenes remains challenging. While photovoltaic cells containing pentacene have demonstrated external quantum efficiencies over 100%,[39,40] these cells employed unique light capture designs to compensate for the mismatch

Received: November 8, 2017
Published: December 14, 2017

DOI: 10.1021/jacs.7b11888
J. Am. Chem. Soc. 2018, 140, 814−826

between pentacene's triplet diffusion length and its light absorption depth.[41] In addition, the low energy of pentacene triplet excitons limits their ability to sensitize many semiconductors employed for photovoltaics, including bulk silicon. Valid concerns also exist regarding the limited photostability of acenes in the presence of oxygen.[42]

In contrast to materials such as tetracene and pentacene, perylenediimides (PDIs) possess many properties that make them particularly well-suited for SF-based light harvesting applications. PDIs possess deep-seated HOMO and LUMO levels, which makes them resistant to photooxidation,[43] and display molar extinction coefficients in the range of $5-10 \times 10^4$ M^{-1} cm^{-1},[44−49] ∼2−10× larger than that of acenes.[32,34,50−52] As a result, PDIs are commonly employed as industrial paints and pigments.[53,54] Importantly, PDI monomers possess a lowest triplet exciton energy measured in the range of 1.10−1.28 eV,[44,46,55] roughly half that of their lowest singlet exciton state, 2.36 eV, suggesting PDIs should be ideal SF chromophores.

This conclusion is supported by calculations that examined intermolecular SF between cofacially arranged PDI dimers.[56−58] However, this work also predicts the rate and yield of SF between dimers depends sensitively on their relative arrangement. PDIs in thin films and molecular crystals tend to pack in cofacial arrangements where their molecular planes are separated by ∼3.5 Å.[59,61,62] At these separations, significant orbital overlap between neighboring PDIs occurs. This produces strong charge resonance interactions that can facilitate direct electron exchange between neighboring PDIs. Such interactions are critical to SF as this process involves, at a minimum, the exchange of two electrons between molecules (Scheme 1).[1] However, the relative strength of these interactions changes rapidly as two PDIs are slipped along both their long and short axes due to the nodal structure of their frontier molecular orbitals.

Scheme 1. Diabatic States That Can Facilitate SF between Two Identical Molecules A and B[a]

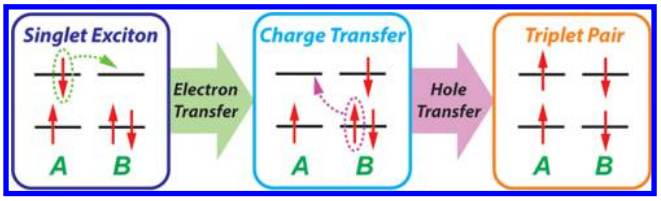

[a]Electron transfer from A to B followed by back electron transfer can prepare a triplet pair state. An analogous path can be drawn where hole transfer from A to B precedes electron transfer.

The impact of charge resonance coupling on SF between PDI dimers has been investigated using models based on both Marcus[57,63] and Redfield theory.[56,58] Both sets of computations predict SF to undergo large variations in rate as one PDI is slipped with respect to its neighbor, with Redfield theory predicting the SF rate to range from 1/25 fs^{-1} to essentially zero as a result of Ångström-scale changes in packing structure (Figure 1).[56] However, each model suggests different maximal rates and ideal geometries for SF. While Redfield theory predicts SF should unfold over femtosecond time scales when PDIs are slipped along their long axis by 2.85 Å,[56] Marcus theory suggests minimizing this slip (0.7 Å) will lead to a SF time scale on the order of hundreds of picoseconds.[57] Although measurements of PDI films have shown they are indeed capable

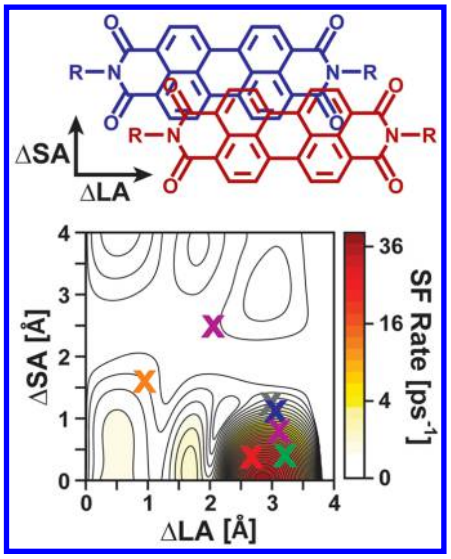

Figure 1. (Top) PDIs form linear columns in the solid state wherein molecules are slipped with respect to one another. The degree of slip between molecules can be adjusted via functionalization at the PDI imide position. (Bottom) Redfield rate calculation showing how the SF rate of two PDIs changes with intermolecular slip.[56] Colored X's represent slip-stacking geometries taken from reported crystal structures of the PDIs in Scheme 2,[59−62] with the exception of C7-PDI whose slip-stacking geometry is estimated in the Supporting Information. Orange: C1-PDI; Purple: C3-PDI; Gray: C7-PDI; Blue: C8-PDI; Green: EP-PDI; Red: MO-PDI. Two X's appear for C3-PDI as its crystal structure has two nonequivalent slip-stacked sites.

of SF,[46,64] a systematic experimental investigation examining how the intermolecular structure of PDI films impacts their SF rate and yield to vet these theoretical approaches is lacking.

In this report, we present time-resolved emission and transient absorption measurements of polycrystalline thin films of six PDI derivatives (Scheme 2) that evaluate their ability to undergo SF. Each derivative features substitutions at their imide positions that cause them to exhibit differing structures in the solid state. The six derivatives we have selected were chosen as their published crystal structures[59−62] adopt values predicted to display SF rates spanning over 2 orders of magnitude, allowing us to directly test current theoretical models for SF.[56−58] We find that while the experimentally measured SF rates for this series track with trends previously predicted using Redfield theory, the rates derived from experiment are ∼3−4 orders of magnitude slower than those predicted theoretically. Using electronic structure calculations based on a Holstein-type Hamiltonian, we argue this discrepancy arises from the presence of electronic coupling in

Scheme 2

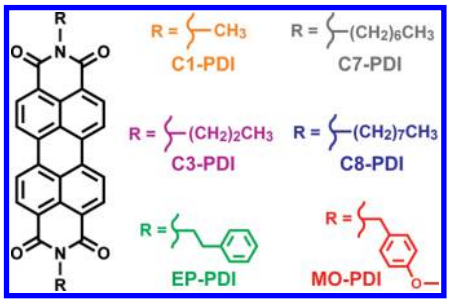

DOI: 10.1021/jacs.7b11888
J. Am. Chem. Soc. 2018, 140, 814−826

the solid state that preferentially lowers the PDI S_1 state energy and introduces an activation barrier for SF. However, despite the presence of this barrier, SF occurs with a ~245 ps time scale in the fastest derivatives we measure. This rate is fast enough to outcompete other singlet deactivation pathways, leading to a high triplet yield of 178%. In extracting this rate, we make note of some pitfalls to avoid when modeling transient kinetics of PDI films. In particular, effects due to nonequilibrium heating of the sample and singlet−singlet exciton annihilation need to be accounted for when extracting SF rates and triplet yields from kinetic data. Interestingly, our results also show triplet excitons formed by SF undergo nonradiative decay to the ground state within ~10 ns, substantially shorter than the ~100 μs lifetime of PDI triplet excitons in solution.[44] This result suggests triplet exciton pairs produced by SF may face difficulty diffusing apart, which must be considered when designing light harvesting applications from these structures.

2. EXPERIMENTAL METHODS

Thin Film Preparation. C1-PDI (*N*,*N*′-dimethyl-3,4,9,10-perylenedicarboximide, 98%), C3-PDI (*N*,*N*′-dipropyl-3,4,9,10-perylenedicarboximide, 97%), C7-PDI (*N*,*N*′-diheptyl-3,4,9,10-perylenedicarboximide, 99%), C8-PDI (*N*,*N*′-dioctyl-3,4,9,10-perylenedicarboximide, 98%), EP-PDI (*N*,*N*′-bis(2-phenylethyl)-3,4,9,10-perylenedicarboximide, 98%), and MO-PDI (*N*,*N*′-bis[(4-methoxyphenyl)methy]-3,4,9,10-perylenedicarboximide, 99%) were each obtained from Sigma-Aldrich and used as received (see Scheme 2 for structures). Polycrystalline thin films of each PDI were grown using a thermal evaporator (AMOD PVD system, Ångstrom Engineering Inc.) operating at room temperature and a base pressure of 10^{-6} to 10^{-7} Torr with a deposition rate of ~1 Å/s. For time-resolved measurements, films were prepared on two different substrates, SiO_2 (glass or fused quartz; Ted Pella Inc.) and c-cut sapphire (Ted Pella Inc.). These substrates have thermal conductivities that differ by an order of magnitude. As we show below, measurements performed on different substrates were necessary to isolate signals from nonequilibrium heating of sample films. Prior to deposition, sample substrates were carefully cleaned by sequential sonication in toluene, chloroform, isopropanol, and acetone for 15 min each. The substrates were subsequently rinsed with methanol and dried with N_2 gas. Following deposition, films were thermally annealed for 2 h at 500 K under pressures of ~10^{-2} Torr in a Janis ST-100 cryostat to increase their average crystallite size.

Film Characterization. Film thicknesses were determined using spectroscopic ellipsometry (M-2000, J. A. Woollam) performed on films deposited on n-type Si(111) grown simultaneously with films deposited on SiO_2 and sapphire. The data was fit using a Cauchy model for the dielectric function from 900 to 1600 nm, where the imaginary part of the dielectric function can be assumed to be zero. These substrates were cleaned by the same method detailed above and have a ~2 nm native oxide coating. Transmission and reflection spectra of PDI films were measured by a Shimadzu UV-2600 UV−vis spectrometer with an integrating sphere attachment. Emission spectra were collected in a front-face geometry following excitation at 402 nm using a Horiba Jobin Yvon Fluorolog3. The mesoscopic structure of sample films was investigated using atomic force microscopy (AFM) and grazing incidence wide-angle X-ray scattering (GIWAXS). AFM images were recorded with an Asylum Research MFD-3D AFM employing an aluminum-coated silicon cantilever (μmasch, HQ:NSC14/Al BS) in tapping mode and analyzed using the Gwyddion software package.[65] GIWAXS out-of-plane patterns were measured using a Rigaku Ultima IV (λ = 1.5461 Å) with a collinear beam at ω = 0.2°.

Transient Absorption. The optical setup used to record transient absorption (TA) spectra with femtosecond time-resolution has been described previously.[64] In brief, the frequency doubled output of a Ti:sapphire amplifier (Coherent Legend Elite Duo, 3 kHz, 4.5 mJ, 90 fs) excited sample films. A white light supercontinuum derived by focusing 0.5−1.0 μJ of the amplifier output into either a flowing water cell or a c-cut sapphire plate (3 mm thickness) formed a time-delayable probe. Pump-induced changes in the probe transmission were detected by spectrally dispersing the probe onto a CCD camera (Princeton Instruments PyLoN 100BR). The time resolution of these experiments was found to be 155 fs based on a cross-correlation measured between the pump and probe using an uncoated sample substrate. TA spectra measured with nanosecond-to-microsecond time delays were recorded using the same white light continuum employed for femtosecond-resolution measurements in conjunction with a 532 nm pump pulse derived from the frequency doubled output of an electrically triggerable Nd:YAG laser (Alphalas Pulselas-A, <1 ns, 8.7 μJ). A digital delay generator (Stanford Research Systems DG535) triggered the pump laser at 1.5 kHz and synchronized its operation with that of the Ti:sapphire amplifier. Femtosecond TA spectra were recorded with the pump and probe oriented at the magic angle (54.7°) while measurements employing nanosecond excitation pulses were performed using perpendicularly oriented pump and probe pulses to reduce signal contributions from scattered pump light. All TA measurements were performed on samples housed in an evacuated Janus ST-100 cryostat with a base pressure of 10^{-2} Torr to prevent oxidative damage of sample films during data collection.

Time-Resolved Emission. Time-resolved photoluminescence of PDI films was measured using a supercontinuum fiber laser (Fianium, SC-450-PP) operating at 1 or 2 MHz as the excitation source. We found the employed repetition rate did not affect the recorded kinetics. Films were excited at 495 nm using ~2 pJ pulses, giving an excitation density 10^{14} to 10^{15} cm^{-3} depending on film absorption and thickness, and a Hamamatsu C10910−04 streak camera was used to collect time-resolved spectra. The instrument response function depends on the time window size, and is ~80−100 ps for 1−2 ns time windows and ~1−2 ns for a 50 ns collection window. Sample data was recorded using a long-pass filter to minimize scattered excitation light. The instrument response function was determined without the filter using scattered excitation light from the film.

3. EXPERIMENTAL RESULTS

3.1. Structural Characterization of Vapor Deposited PDI Films. Following vapor deposition of PDI films, AFM was used to characterize their structure. Figure 2 displays AFM images of three representative PDI films, C3-PDI, C7-PDI, and

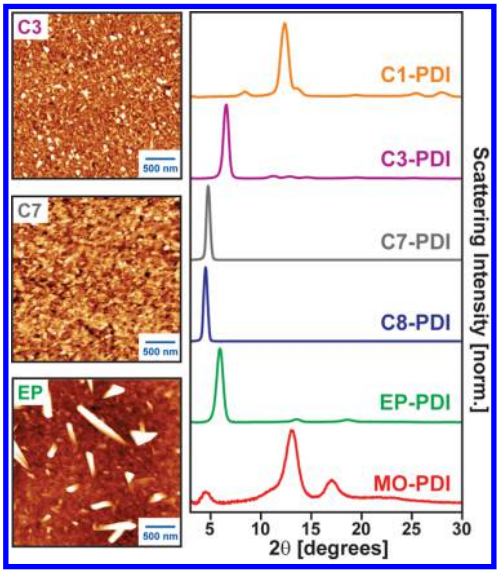

Figure 2. (Left) AFM images of C3-PDI, C7-PDI, and EP-PDI films showing they are comprised of crystalline grains. (Right) GIWAXS patterns of PDI films confirm that PDIs within these grains adopt structures similar to those reported for single PDI crystals.

DOI: 10.1021/jacs.7b11888
J. Am. Chem. Soc. 2018, 140, 814−826

EP-PDI, on sapphire substrates. Images of C1-PDI, C8-PDI, and MO-PDI films on sapphire appear in Figure S1 of the Supporting Information. Needle-like features can be seen in each image, indicating they are comprised of numerous grains with differing orientations that range in length from 50 nm to 1 μm. To determine the structure of the grains within each film, we recorded the GIWAXS patterns of PDI films deposited on sapphire substrates (Figure 2). Comparison of measured patterns and predicted powder X-ray diffraction patterns based on reported PDI single crystal structures[59−62] show agreement in the overall placement of peaks (Supporting Information, Figure S1), indicating the grains observed in AFM images adopt structures similar to those reported for single crystals. However, several peaks expected for randomly oriented crystallites are suppressed or absent in the experimental data, indicating our films are highly textured. At first glance, the diffractograms of C3-PDI, C7-PDI, C8-PDI, and EP-PDI suggest crystallites orient such that the long-axis of the PDI cores are situated mostly perpendicular to the substrate, while those of C1-PDI and MO-PDI lie nearly parallel with the substrate plane. A more detailed analysis of crystallite orientation is underway for a future study. While our GIWAXS and AFM images indicate our films do contain heterogeneity, overall we find crystallites adopt structures similar to those of reported bulk crystals,[59−62] thereby allowing us to examine how intermolecular packing impacts the rate and yield of SF.

Solution-phase absorption spectra of the six PDIs we have investigated are shown in Figure S2 of the Supporting Information. When dissolved in dichloromethane, the absorption spectrum of each PDI is nearly indistinguishable from each other, highlighting that substitutions at the PDI imide position have a negligible impact on their frontier molecular orbitals.[49] These spectra show a characteristic vibronic progression with an energy spacing of ∼1355 cm^{-1} associated with ring stretching modes of the central perylene chromophore. Steady-state fluorescence spectra for dilute PDI solutions display small Stokes shifts and largely mirror features seen in the absorption data.

In sharp contrast, absorption and emission spectra measured for vapor deposited PDI films display features that vary strongly along the series we have investigated (Figure 3). These spectral differences arise from strong intermolecular coupling in the solid state. Interestingly, while PDIs such as C7-PDI (gray) and C8-PDI (blue) display a relatively small absorption bandwidth with an absorption maximum blue-shifted relative to the 0−0 absorption transition, other PDIs, such as EP-PDI (green), show a larger absorption bandwidth containing two distinct bands centered near 460 and 620 nm. For each PDI film, the emission spectrum is red-shifted and broadened relative to that of solution-phase PDIs and have significantly modified vibronic progressions.

The presence of both blue-shifted absorption bands and red-shifted emission suggests excitonic states in PDI thin films cannot be described as prototypical H- or J-aggregates. Within the 1D slip-stacked columns that comprise crystallites in PDI films investigated here, neighboring molecules are closely arranged, with only ∼3.5 Å between their molecular planes. This close arrangement induces significant orbital overlap between neighboring molecules, giving rise to non-negligible short-range charge transfer (CT) couplings on par with the magnitude of long-range Coulombic couplings associated with H- or J-aggregate formation.[66] Moreover, due to the nodal structure of a PDI's frontier molecular orbitals, the sign and

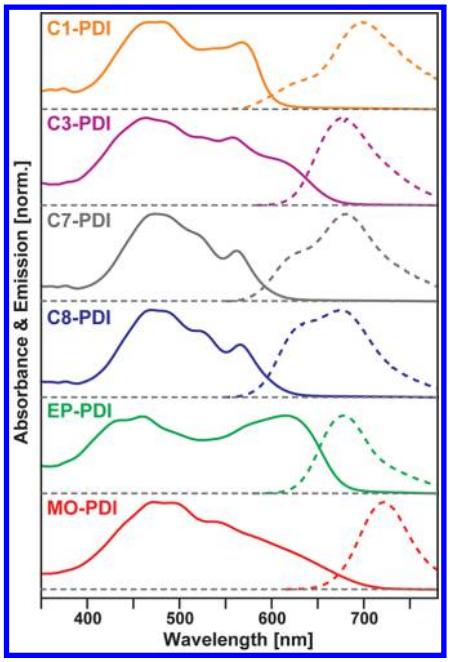

Figure 3. Absorption (solid lines) and emission spectra (dashed lines) collected following excitation at λ_{Ex} = 402 nm. Plotted absorption spectra are for films grown on sapphire substrates, while emission data is for films grown on glass.

magnitude of the CT couplings vary substantially as two neighboring PDIs are slipped cofacially.[67] Spano and co-workers have investigated how both CT and Coulombic coupling impact optical spectra of PDI crystals and concluded their absorption bandwidth reflects the relative sign and magnitude of these interactions.[68−70] For the PDIs we investigate here, Coulombic coupling is expected to lead to H-type aggregate behavior and a characteristic blue shift of their absorption bands. However, the significant red-shifted and large absorption bandwidth of EP-PDI is indicative of strong J-type CT couplings that oppose Coulombic H-type coupling. The comparatively small absorption bandwidth of C7-PDI and C8-PDI results from weak CT coupling that allows Coulombic interactions to have a proportionately greater influence on their spectra.

Strong CT couplings in EP-PDI may lead to an increased SF rate as CT states are believed to play a key role mechanistically. One mechanism by which SF can proceed is via the formation of a CT intermediate followed by back electron transfer to form a correlated triplet pair (Scheme 1).[1,2,71] Participation of the CT intermediate in Scheme 1 as a real[72,73] or virtual configuration[74,75] likely varies between systems. Regardless, tuning the CT couplings that dictate the absorption profiles in Figure 2 should impact the SF rate of PDI films. This prediction is largely captured by Redfield theory simulations investigating SF between PDI dimers.[56] Molecules in Scheme 2 with significant CT couplings, based in part upon the breadth of their absorption bands (Figure 3), are predicted to display the fastest SF rates (Figure 1). However, this expectation must be tempered as the absorption edge of each PDI film is red-shifted from the 0 → 0 transition of PDI molecules in solution, indicating Coulombic and CT coupling can decrease the PDI S_1 energy in thin films. As we argue below, this introduces an activation barrier for SF, suggesting electronic coupling must be managed in order to simultaneously maintain a reasonably large

DOI: 10.1021/jacs.7b11888
J. Am. Chem. Soc. 2018, 140, 814−826

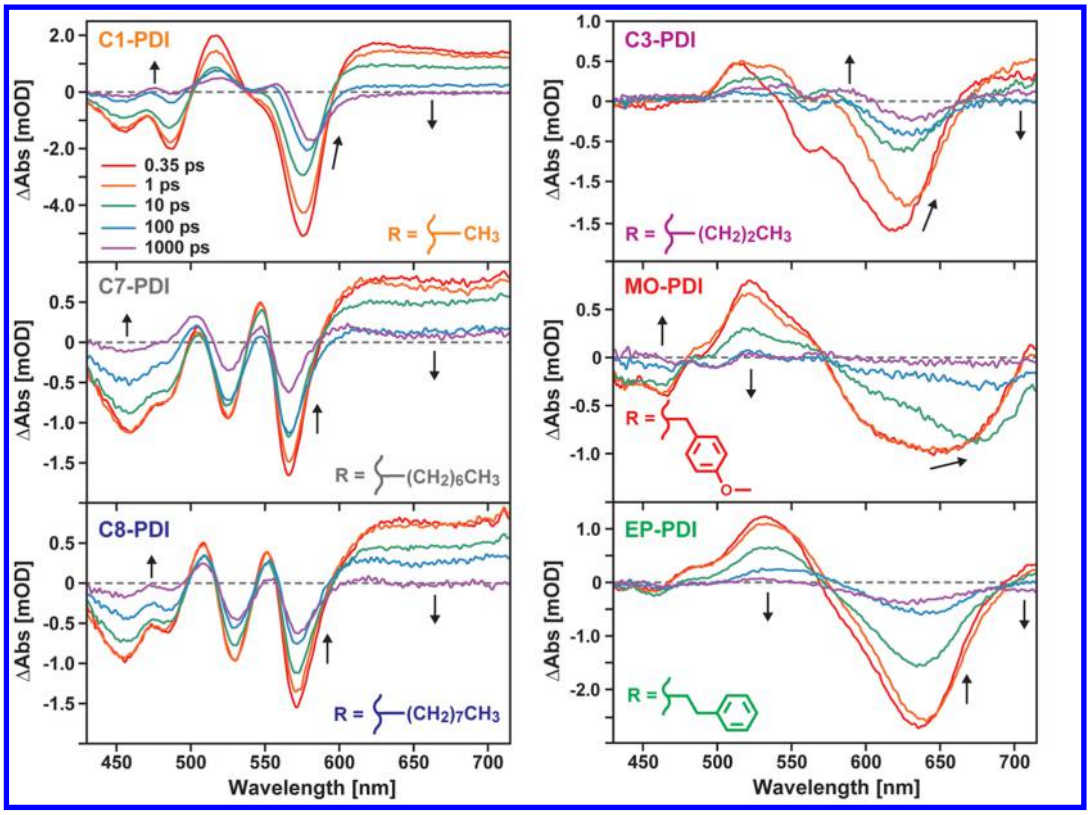

Figure 4. TA spectra of PDI films measured following excitation at 400 nm. Arrows denote the direction of band changes seen following photoexcitation. Plotted spectra were recorded for films thermally annealed on sapphire substrates.

SF coupling and an energetic balance between singlet and triplet exciton states to ensure efficient SF.

3.2. Triplet Exciton Production. To determine the presence of SF in vapor deposited PDI films, TA measurements employing a 400 nm excitation pulse were used to track their excited state dynamics. Figure 4 contains representative TA spectra of films of the six PDIs in Scheme 2, highlighting their evolution over hundreds of femtoseconds to one nanosecond. Spectra measured shortly after photoexcitation (Δt = 0.35 ps) have distinctive features that can broadly be grouped into one of two categories. C1-PDI, C7-PDI, and C8-PDI films each exhibit a narrow ground state bleach (GSB) centered around 570 nm (Figure 4, left column), while C3-PDI, EP-PDI, and MO-PDI display a broad, lower energy bleach near 600−700 nm (Figure 4, right column). These variations in the position of the GSB reflect differences in the absorption onset for each PDI film (Figure 3).

While C1-PDI, C7-PDI, and C8-PDI possess absorption profiles with relatively narrow line widths and absorption maxima to the blue of 600 nm, C3-PDI, EP-PDI, and MO-PDI each exhibit broad absorption bands with onsets extending well to the red of 600 nm. As discussed above, these line shape differences reflect the presence of stronger CT coupling between molecules within C3-PDI, EP-PDI, and MO-PDI films with respect to C1-PDI, C7-PDI, and C8-PDI films.

In addition, a broad induced absorption is observed to the red of the GSB upon photoexcitation. As the induced absorption rises within the instrument response of our TA spectrometer, we assign this feature to the photoexcited singlet exciton state. Within the first few picoseconds following excitation, evolution of the GSB and induced absorption occurs, but have minimal impact on their overall spectral profiles. As such, we assign this evolution to cooling of excited singlet excitons due to movement away from the Franck−Condon region. Over longer time scales of tens to hundreds of picoseconds, the singlet excited state absorption for each PDI decays to baseline. Concurrent with this decay, we observe a large decrease in the amplitude of the GSB. However, new absorption bands appear that overlap with the GSB as this decay occurs. For example, C7-PDI and C8-PDI show the growth of a new band at 510 nm, while C3-PDI displays a new feature at 570 nm. The appearance of these bands strongly alters the TA lineshapes for each PDI, suggesting the creation of a new species.

To identify the state produced from photoexcited singlet excitons, we compare our spectra against known spectral features for other excited PDI species. One possible decay path is charge separation resulting in the formation of PDI radical cations and anions.[73,76−79] However, PDI anions are known to display absorption bands in the near-infrared.[80−82] Our spectra lack absorptive transitions in this spectral range following singlet decay (Supporting Information, Figure S3), suggesting radical species do not contribute to our data. Low-energy states with strong excimer character are another species we have considered as geometric relaxation to form such states has been observed in other rylene systems.[83−87] However, the formation of such states is typically signaled by the appearance of prominent near-infrared absorptions and a time-dependent red shift of emission bands. As time-resolved emission traces of our PDI films display minimal spectral evolution and TA spectra do not develop prominent near-infrared induced absorption bands, we too rule out this scenario. Rather, the evolution we observe in TA spectra is consistent with triplet exciton formation. Prior investigations of PDIs have revealed their triplet induced

DOI: 10.1021/jacs.7b11888
J. Am. Chem. Soc. 2018, 140, 814−826

absorption bands overlap considerably with their ground state absorption spectra,[44−46,55,64] suggesting the loss of GSB we observe results from the growth of triplet excitons rather than the return of population to the ground state.

To verify if triplet excitons are being produced in PDI films, we prepared films of each of the six PDIs in Scheme 2 doped with 11% copper(II)phthalocyanine (CuPc). In these films, CuPc acts as a triplet sensitizer that intersystem crosses on a subpicosecond time scale[88,89] to produce triplet excitons that can pass from CuPc to the PDI host matrix.[33,64,90] Using a home-built noncolinear optical parametric amplifier (NOPA) as an excitation source, we measured TA spectra of CuPc-doped PDI films following selective excitation of CuPc at 690 nm. From this data, we used a previously described methodology[64] to extract the TA spectral component arising from PDI triplet excitons. Figure 5 compares triplet spectra against TA data

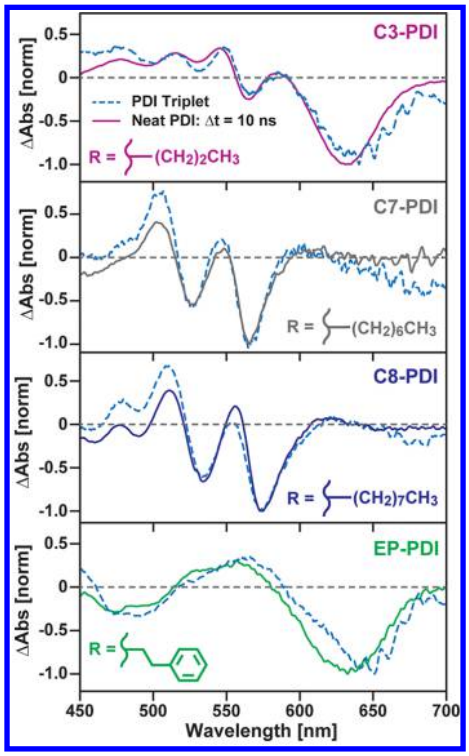

Figure 5. Comparison of TA lineshapes measured for C3-PDI (purple), C7-PDI (gray), C8-PDI (blue), and EP-PDI films (green) to transient lineshapes obtained from triplet sensitization (dashed light blue).

measured for neat PDI films. For C3-PDI, C7-PDI, C8-PDI, and EP-PDI films, the sensitized triplet spectra are found to be in excellent agreement with spectra measured for each film following a 10 ns time delay, indicating triplet excitons are the dominant species populated at this delay. Similar sensitization experiments were performed on MO-PDI films, but proved inconclusive as overlapping absorption by MO-PDI and CuPc prevented selective excitation of CuPc. However, TA spectra of neat MO-PDI films display induced absorption bands at 525 and 565 nm, similar to EP-PDI triplet excitons. Thus, we assign this feature to the MO-PDI triplet exciton. Given the fluorescence quantum yield and emission lifetime of PDI monomers in solution is >97% and 3.7−4.3 ns,[44,64] the upper bound on the rate for PDI intersystem crossing is 1/120 ns^{-1}. We expect this rate to change minimally when moving from solution phase to crystalline environment. Thus, the appearance of triplet excitons on time scales of a few nanoseconds or less following photoexcitation strongly suggests they result from SF.

3.3. Triplet Exciton Relaxation. To determine the lifetime of triplet excitons produced by SF, a white light continuum derived from a Ti:sapphire amplifier was used to probe changes in the absorption of PDI films induced by 532 nm pulses produced by an electrically trigerable frequency-doubled Nd:YAG laser. Figure 6 displays TA spectra of C7-PDI and

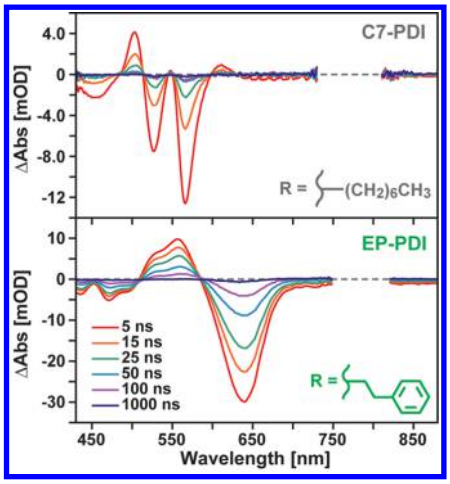

Figure 6. TA spectra of C7-PDI and EP-PDI films measured for nanosecond-scale time delays following photoexcitation at 532 nm. Data recorded for probe wavelengths near the 800 nm fundamental used to generate the white light continuum probe are omitted due to excessive noise. Plotted spectra are for PDI films grown on sapphire substrates.

EP-PDI films measured using this setup for pump−probe time delays extending out to 1 μs. Analogous spectra for C1-PDI, C3-PDI, C7-PDI, and MO-PDI appear in Figure S3 of the Supporting Information. Spectral changes in the TA line shape of each PDI film are minimal beyond a time delay of 5 ns, indicating triplets are the dominant end species formed following photoexcitation. Over time, the amplitude of triplet TA features decays, with the majority relaxing over tens of nanoseconds. This relatively fast loss of triplet amplitude is unexpected given the lifetime of PDI triplet excitons in dilute solution is on the order of 100 μs.[44,45,91] Our data indicates triplets produced via SF in PDI films access a decay pathway that does not exist in dilute PDI solutions. While the rate of the observed decay does vary with PDI structure, each film undergoes nearly complete relaxation to the ground state within ~50 ns. We note we have been careful to perform TA measurements in an evacuated cryostat to minimize triplet quenching by oxygen. Data in Figure 6 was also recorded for PDI films grown on sapphire substrates to minimize contributions stemming from photoinduced heating of sample films (see Supporting Information, Section SIII).

We note the rapid decay of triplet excitons we observe differs somewhat from prior work investigating SF in polycrystalline thin films of *N*,*N*-bis(*n*-octyl)-2,5,8,11-tetraphenyl-PDI (Ph_4-PDI).[46] SF in Ph_4-PDI was reported to produce a 140% yield of triplet excitons 60 ns after photoexcitation whereas our PDI film data shows their triplet populations have largely returned to the ground state by this delay. The differences in triplet lifetime we and ref 46 report could be tied to differences in the average size of polycrystalline grains within films as well as

DOI: 10.1021/jacs.7b11888
J. Am. Chem. Soc. 2018, 140, 814−826

differences resulting from the addition of conjugated substituents to the bay positions of Ph_4-PDI. However, we note the high triplet yield reported for Ph_4-PDI films was determined by examining the amplitude of the film's photobleach signal after a 60 ns time delay. We caution using this approach as photobleaching signals can also arise from photoinduced heating of sample films by the laser pulses employed for TA. As we[64] and others[92,93] have previously reported, photoinduced heating of ground state molecules can shift their spectra, giving rise to a transient spectral signature resembling the difference between the absorption spectrum of a sample measured at low and high temperature.

As we show in Section SIII of the Supporting Information, contributions to TA spectra from photoinduced heating can be clearly identified by comparing measurements of films deposited on substrates with different thermal conductivities, such as quartz and sapphire. The origin of the thermal background has several sources: exciton cooling on the S_1 potential energy surface, singlet and triplet exciton decay, and singlet−singlet exciton annihilation, which occurs due to the high excitation densities employed for TA measurements (Supporting Information, Figure S4). As background signals contain a contribution from the PDI GSB, using the GSB to quantify triplet yields must account for thermal contributions to the total measured signal.

3.4. Tracking SF Dynamics with Time-Resolved Photoluminescence. While TA spectra confirm PDI films undergo SF, quantitatively extracting SF rates, triplet yields, and triplet recombination time scales from this data is complicated by signal contributions from both photoinduced heating and singlet−singlet exciton annihilation. In part, these obfuscating spectral signals arise from the high excitation densities employed for TA. In contrast, time-resolved emission measurements use lower excitation densities that can mitigate both effects. For this reason, we have measured time-resolved emission decay profiles of each of our PDI films, which we quantitatively model in Section 4 below to discern how changes in PDI film structure influence their SF rate and yield.

Figure 7 displays time-resolved emission profiles for polycrystalline films of three of the six PDIs whose structures appear in Scheme 2. Emission profiles for other PDIs appear in Figure S7 of the Supporting Information. While emission traces measured for each PDI in solution yield nearly identical monoexponential decays that can be fit with a 4.1−4.4 ns time constant (Supporting Information, Table S1), emission decays measured for each film display multiexponential kinetics whose time constants vary by more than an order of magnitude across the series of films investigated. Interestingly, emission spectra of PDI films display minimal line shape changes with time-evolution (Figure S6). This suggests emission originates from the S_1 state despite the observation of multiple relaxation time scales. However, one exception to this observation is C1-PDI, whose emission spectrum shifts to lower energy by ∼80 meV over 700 ps, indicating emitting species gradually relax to lower energies in this material. While the average emission decay rates for each PDI film are accelerated relative to PDI monomers in solution, each displays a small, long-lived emission component that persists for a few nanoseconds to tens of nanoseconds, suggesting this emission originates from a process other than PDI monomer relaxation. Our TA measurements reveal PDI triplet excitons undergo relaxation on a similar time scale, suggesting singlet excitons giving rise to this delayed emission are formed from triplets. Indeed, delayed emission stemming from singlet excitons produced by triplet recombination is a hallmark of many SF materials.[25,29,30,64,94]

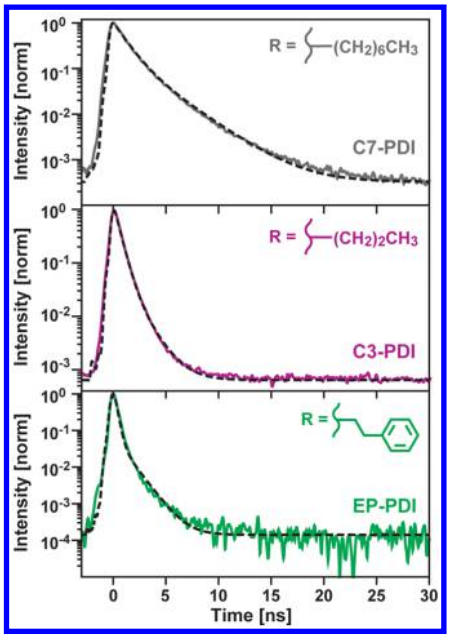

Figure 7. Time-resolved emission kinetics of polycrystalline C7-PDI (gray), C3-PDI (purple), and EP-PDI (green) films measured following photoexcitation at 495 nm. Plotted data was recorded using a streak camera and is spectrally integrated from 675 to 740 nm. Fits to the data based on the kinetic model described in Section 4.1 are overlaid (dashed black).

Interestingly, we find PDIs that display the fastest emission decays are those that adopt slip-stacking structures predicted to maximize their SF rate. Looking across the emission series in Figures 7 and S7, the primary decay component of each PDI accelerates moving from C8-PDI to C3-PDI to MO-PDI. This is consistent with the trend predicted by the Redfield model in Figure 1,[56] which suggests PDIs with a large degree of slip along their long axes and minimal slip along their short axes, such as MO-PDI, should undergo SF more readily than PDIs that adopt different geometries, such as C8-PDI. However, while the general trend of predicted SF rates in Figure 1 appears to be reflected in the decay profiles in Figure 7, the overall magnitude for the predicted decay rates differs substantially between theory and experiment. Redfield theory predicts SF to occur on time scales stemming from ∼50 fs to a few picoseconds, yet the fastest decay kinetics we observe unfold over hundreds of picoseconds. As we describe below, we ascribe this discrepancy between theory and experiment to the introduction of a thermal activation barrier for SF due to a lowering of the PDI S_1 state energy in films due to electronic coupling.

4. DISCUSSION

4.1. Modeling SF Kinetics in Polycrystalline PDI Films. Combined, our TA and time-resolved emission data suggest the polycrystalline PDI films we have studied undergo SF, albeit with rates that differ substantially based on the ordering of molecules within each film. Interestingly, while calculations of PDI dimers[56] predict SF should occur with rates as fast as 1/50 fs^{-1} and 1/40 fs^{-1} for EP-PDI and MO-PDI respectively, our TA spectra (Figure 4) and time-resolved emission data (Figures 7 and S7) display drastically slower kinetics that unfold over

DOI: 10.1021/jacs.7b11888
J. Am. Chem. Soc. 2018, 140, 814−826

hundreds of picoseconds. To quantitatively extract SF rates from this data for comparison to theory, we have fit the emission decay curves in Figures 7 and S7 to a kinetic model that accounts for SF, triplet fusion, and relaxation of singlet and triplet excitons to the ground electronic state (Figure 8). Prior

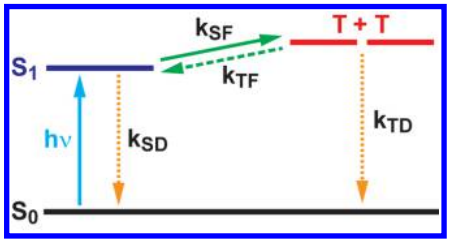

Figure 8. Jablonski diagram illustrating the kinetic model used to fit time-resolved emission from PDI films. Differential equations describing the population of each state are provided in the Supporting Information.

work by our group has shown contributions from singlet–singlet exciton annihilation and photoinduced heating of PDI films can lead to time-dependent absorptivity changes that must be accounted for when fitting TA spectra.[64] For this reason, we have elected to fit our time-resolved emission data, rather than our TA spectra, as the emission data is minimally impacted by these effects.

In our kinetic scheme, photoexcited PDI molecules are initially placed in a singlet excited state that can either decay to the ground state through a combination of radiative and nonradiative paths (k_{SD}) or undergo SF to form a pair of triplet excitons (k_{SF}). In our model, we make no distinction between the so-called triplet pair state, ^{1}(TT), and independent triplets as we do not observe spectroscopic evidence for the existence of two distinct triplet subpopulations. While recent work examining SF in acene thin films,[95] aggregates,[96] and single crystals[97] has suggested the ^{1}(TT) state is a distinct entity that can be identified either through unique spectroscopic signatures or kinetic changes in triplet production rate, in the PDI films we have investigated we can adequately reproduce our results by postulating the existence of a single time scale that interconverts singlet and triplet population.

Once formed, triplets can either recombine to reform singlet excitons (k_{TF}) or undergo nonradiative decay to the ground state (k_{TD}). Triplet excitons that recombine are taken to form singlet excitons exclusively as TD-DFT calculations have suggested triplet recombination to form a higher energy triplet state is energetically unfavorable.[46,71] Properly describing the recombination of triplet exciton pairs requires not only accounting for the rates of different photoconversion processes but also the three-dimensional spatial diffusion of triplet excitons following their formation.[98] While some triplet pairs will reencounter one another multiple times and eventually recombine, others can diffuse apart and decay independently. Rather than explicitly model the spatial diffusion of triplet excitons within films, we employ a coarse-grained approach we have previously shown can quantitatively reproduce dynamics observed in C8-PDI films.[64] Specifically, we approximate the dynamics associated with triplet separation by dividing triplet exciton pairs into two populations, one that recombines to form singlet excitons, and a second population wherein the triplets diffuse far enough apart that they independently return to the ground electronic state. Rates describing the recombination and decay of these two populations, respectively, are taken to follow first-order kinetics.

Differential equations describing the time-dependent singlet and triplet populations described by this model are given in Section SV of the Supporting Information. While our model is minimal, it does contain 5 parameters to be determined: the relaxation rates for singlet and triplet excitons (k_{SD} and k_{TD}), the percentage of triplets that recombine ($\mathcal{F}_{recomb}$), and the SF and triplet fusion rates (k_{SF} and k_{TF}). To reduce the number of free parameters in our fits, we have constrained the value of k_{TD} to match the decay rates observed for triplet excitons in TA measurements (Figure 6). Fits to time-resolved emission traces with this constraint in place are shown as dashed black lines alongside the experimental data shown in Figure 7. For all films investigated, apart from C1-PDI, the fits well-reproduce the measured emission traces. We have also verified the SF rates derived from our model have minimal dependence on parameters describing triplet exciton recombination. As previously noted, C1-PDI films display a shifting of their emission spectra to lower energy following photoexcitation not observed in other PDI films (Figure S6). This shifting contributes an additional kinetic rate not captured by our model and as a result we refrain from reporting rate constants derived from our kinetic model for C1-PDI. Nevertheless, for the other 5 PDI films, the minimalistic model in Figure 8 is sufficient to reproduce their emission dynamics.

Table 1 displays kinetic parameters derived from fits to the emission data in Figures 7 and S7. Examining values extracted

Table 1. Best-Fit Parameters for the Kinetic Model in Figure 8 Extracted by Fitting Time-Resolved Emission Profiles for PDI Films[a]

	$1/k_{SF}$ [ns]	$1/k_{recomb}$ [ns]	$1/k_{SD}$ [ns]	$\mathcal{F}_{recomb}$ [%]	$1/k_{TD}$ [ns]	max triplet yield [%]
MO-PDI	0.23	1.04	4.10	6.1	9.8	173
EP-PDI	0.26	1.05	4.17	8.1	28.0	178
C3-PDI	0.61	1.44	4.06	6.1	9.8	151
C7-PDI	1.76	2.49	4.14	18.4	10.0	101
C8-PDI	3.03	1.99	4.11	14.8	8.9	80

[a]We note the SF time scale we report here for C8-PDI slightly differs from that we reported previously ($1/k_{SF}$ = 3.8 ns)[64] as the model used to fit emission data in our prior work postulated triplet exciton decay was negligible on nanosecond time scales.

for the SF rate, we find they span just over an order of magnitude, with the slowest PDIs producing triplets over a few nanoseconds (C8-PDI, $1/k_{SF}$ = 3.03 ns), whereas the fastest PDIs undergo SF on time scales of a few hundred picoseconds (MO-PDI, $1/k_{SF}$ = 231 ps). While this range of rates is noticeably slower than those reported for acenes such as pentacene,[27,99] hexacene,[28] and their derivatives,[100,101] which undergo SF on subpicosecond time scales, the lack of competing singlet exciton deactivation paths in PDI films allows them to exhibit an appreciably high triplet yield despite their slower overall SF rates. This is illustrated in Figure 9, which plots the time-dependent triplet population extracted from our kinetic model. Examining these traces, we find the triplet population reaches a maximum yield of 178% for EP-PDI ~ 2 ns following photoexcitation.

DOI: 10.1021/jacs.7b11888
J. Am. Chem. Soc. 2018, 140, 814–826

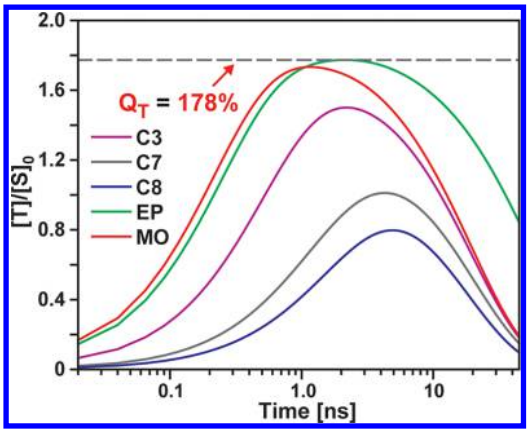

Figure 9. Triplet exciton population extracted from our kinetic model for PDI films, which predicts a maximum triplet yield of 178% for EP-PDI films.

Unfortunately, over tens of nanoseconds, the triplet population produced by SF decays to the ground state, limiting the amount of time available to utilize these excitations for light harvesting applications. Interestingly, while triplet lifetimes reported for tetracene single crystals fall in the range of tens to hundreds of μs,[102−106] triplet exctions produced by SF in polycrystalline tetracene films display lifetimes of 20−100 ns[107] that are much closer to the values we obtain for polycrystalline PDI films. Similarly, while some covalently tethered acenes that undergo intramolecular SF display triplet relaxation time scales >100 ns,[35,37] many do not and triplet lifetimes can be as short as ∼1 ns in these systems.[32,33,38] In carotenoids, triplet pair decay is even faster, occuring over tens of picoseconds.[8,9] These results, in addition to our own, indicate triplet pairs produced by SF can decay to the ground state. The probability of this process appears to be enhanced by spatial confinement of the triplet pair. In systems such as tetracene single crystals, where defects are minimal, triplet pairs likely diffuse apart, minimizing their recombination. Indeed, long triplet diffusion lengths have been reported for single crystal tetracene[108] and rubrene,[109,110] while grain boundaries in polycrystalline tetracene films stymie triplet diffusion.[111] As such, grain boundaries in polycrystalline PDI films may be responsible for the short lifetimes we observe.

Alternatively, the rapid decay of triplet excitons could arise from a binding energy that prevents triplet pairs from separating once formed. Recent work examining acenes in solution and thin films has suggested that the triplet pair state, ^{1}(TT), formed by SF can experience a binding energy of nearly 200 meV.[95] Nonzero binding energies for the ^{1}(TT) state have also been estimated for acene crystals and synthetic dimers on the basis of RAS-2SF calculations and range from tens to a few hundred meV.[112,113] The presence of a similar exciton binding energy between triplet pairs in PDI films could slow triplet separation and enhance decay. Interestingly, we do find EP-PDI displays a triplet relaxation time scale ∼3× longer than other PDIs we have investigated. We are currently working to determine if this longer triplet lifetime results from mesoscopic differences in the structure of PDI films, a reduction in the strength of triplet pair binding, or other effects.

4.2. SF Rate Dependence on Intermolecular Structure. Previous studies have used both Marcus[57] and Redfield[56] theory to predict how the SF rate for a PDI dimer varies with intermolecular geometry. While both sets of calculations found this rate to vary strongly as one PDI is slipped with respect to the other, each predicts different optimal structures to maximize SF. In Figure 10, we compare the rates predicted

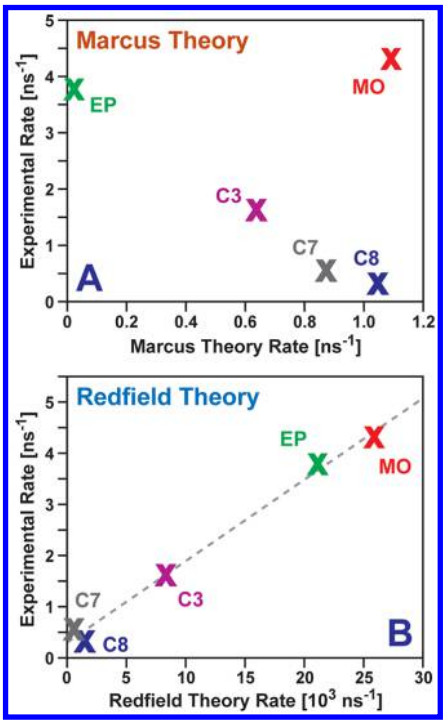

Figure 10. Comparison of SF rates calculated from (A) Marcus and (B) Redfield theory and experimental SF rates for PDI films. Redfield rates taken from ref 56.

by these two sets of calculations against our experimentally determined SF rates. Overall, we find Marcus theory does a poor job predicting which PDIs will display the fastest SF rates (see Section SVIII of the Supporting Information for computational details). While EP-PDI displays one of the fastest experimental SF rates, the Marcus rate model predicts it should be the slowest of the series of PDIs we have investigated.

In contrast, we find a strong positive correlation between the experimentally measured SF rate and that predicted by Redfield calculations (Figure 10B). Redfield theory allows CT states to facilitate SF via superexchange, highlighting the importance of this mechanism. This model predicts slipping PDIs along their long axis by ∼3 Å with minimal displacement along their short axis should maximize their SF rate.[56] Indeed, PDIs such as MO-PDI and EP-PDI, which exhibit minimal short axis displacements and long axis displacements of 2.67 and 3.20 Å respectively,[59] display the fastest SF rates. However, while the theoretical model correctly predicts the experimental trend in observed rates, the values of the calculated rates are ∼3 orders of magnitude larger than experiment. Hence, while our data indicates dimer calculations can be used to determine trends in how SF rates vary with intermolecular geometry, caution must be exercised in using such calculations for quantitative rate predictions.

The Redfield model included in ref 56 considered how different slip-stacking geometries alter the electronic couplings between neighboring PDIs, but not the influence these couplings have on their singlet energy. However, the absorption and emission data in Figure 3 as well as work by others[67−70] indicate the singlet energy of cofacially arranged PDIs differs

DOI: 10.1021/jacs.7b11888
J. Am. Chem. Soc. 2018, 140, 814−826

strongly from that of monomeric PDIs in solution due to both Coulombic coupling as well as CT interactions. These couplings cause singlet excitons in PDI molecular crystals to delocalize over multiple molecules, and tend to lower their overall energy relative to PDI monomers. In contrast, PDI triplet excitons are expected to be perturbed less when moving from solution to a molecular crystal as through-space Coulombic coupling is forbidden for these excitations.[114] While the energy splitting between PDI singlet and triplet exciton states for PDI monomers is ideal for SF,[44,56] preferential stabilization of PDI singlet excitons in the solid state can produce an appreciable thermal activation barrier for SF. Indeed, introducing a modest activation barrier of 200 meV into an Arrhenius rate expression would slow the rate by a factor of 3×10^{-4} at room temperature, a change of the same order of magnitude as the discrepancy we find in our measured experimental rates and those predicted by Redfield theory.[56]

To evaluate how intermolecular coupling influences the thermodynamic driving force for SF, we have used a Holstein-type Hamiltonian approach[68−70] to estimate how the S_1 and T_1 state energies of PDI monomers change when they are arranged into cofacial 1D columns with differing degrees of slip displacement. We direct interested readers to the Supporting Information for a detailed description of this model. In brief, this approach accounts for both Coulombic and CT coupling between neighboring PDIs as well as contributions from the dominant C═C stretching mode that modulates the absorption spectrum of PDI monomers.

Figures 11A and 11B display contour maps showing how the S_1 and T_1 state energies change with intermolecular slip. Examining the SF rates predicted in Figure 1, we see PDIs that experience no slip along their short axis and a long axis slip of 2.85 Å are expected to display the fastest SF rates. Interestingly, the calculated state energies in Figures 11A and 11B show intermolecular displacements of this type strongly perturb both the S_1 and T_1 state energies, lowering their values compared to those of PDI monomers. This is perhaps not surprising. Within a CT-mediated picture for SF, both the electron and hole exchange integrals between neighboring molecules directly contribute to the SF rate. These same exchange integrals are also responsible for the CT-mediated couplings that shift the energies of exciton states described by a Holstein-type Hamiltonian. Importantly, the absence of long-range Columbic coupling between triplet exciton levels causes the S_1 state energy to be lowered more than that of the T_1 state, introducing an activation barrier of ∼190 meV for SF.

Figure 11C plots how this activation barrier changes with intermolecular geometry. Shifts in the S_1 and T_1 state energies are highly correlated, albeit with smaller overall shifts for the T_1 state energies. This leads to relatively small changes in the SF activation energy, which varies from only 174 meV for C7-PDI to 232 meV for EP-PDI despite the vastly different intermolecular couplings calculated for crystals of these materials. This relatively modest variation in activation energy with intermolecular geometry likely leads to the nearly constant reduction in the experimental SF rate relative to predictions of the Redfield model in ref 56. (Figure 10B). Our results highlight the importance of considering not only the electronic coupling between neighboring molecules when predicting SF rates, but also the impact these couplings have on the relative energies of the singlet and triplet exciton states that participate in SF. While strong coupling generally speeds SF, it can also introduce a thermal activation barrier that needs to be overcome to produce triplet exciton pairs.

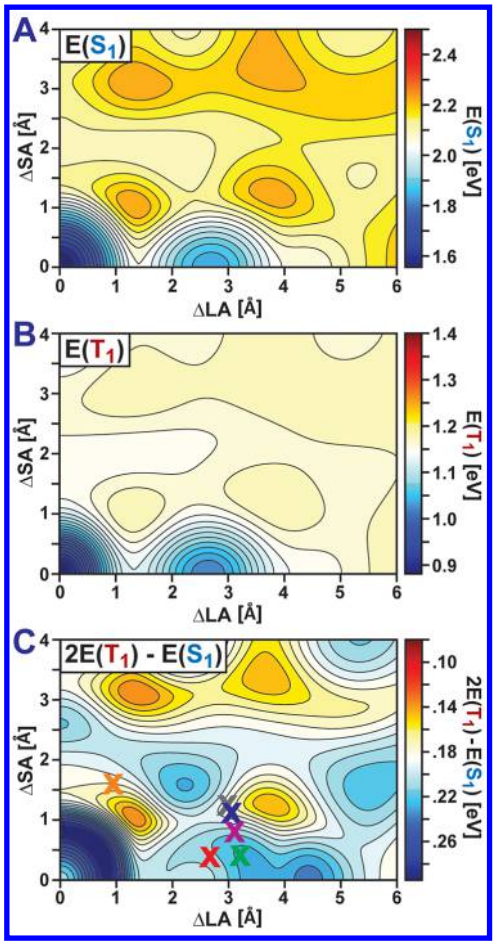

Figure 11. (A,B) Geometric dependence of the energies of the lowest singlet (A) and triplet exciton (B) states computed from a Holstein-type Hamiltonian. (C) Activation energy for SF estimated from this model. ΔSA and ΔLA denote the degree of slip between neighboring PDIs in the model, as defined in Figure 1. The spacing between neighboring PDIs was held at 3.5 Å for these calculations. Colored X's in panel C denote slip-stacking geometries for the PDIs we investigate. Orange: C1-PDI; Purple: C3-PDI; Gray: C7-PDI; Blue: C8-PDI; Green: EP-PDI; Red: MO-PDI.

5. CONCLUSIONS

Due to their overall good photostability, high extinction coefficients, and ease of processability, PDIs are appealing chromophores for SF-based applications. The strong dependence of CT-mediated couplings on the displacement of neighboring PDIs within slip-stacked columns makes the overall rate and yield of SF highly sensitive to thin film structure. When PDIs are arranged cofacially with a slip along their long axis of ∼3 Å and minimal short axis slip, triplet excitons can be produced with 178% yields over ∼245 ps. This rate, which is slower relative to other SF materials such as pentacene and hexacene, results as the strong CT couplings that facilitate SF in PDI films also conspire to induce a thermal activation barrier of ∼190 meV. Following their formation, triplets return to the ground state over tens of nanoseconds. Optimization of film structure to prolong the lifetime of triplet excitons is the next key challenge for the development of PDI-based SF materials. Nevertheless, the high triplet yields we have

DOI: 10.1021/jacs.7b11888
J. Am. Chem. Soc. 2018, 140, 814−826

obtained demonstrate PDIs are promising materials for commercial SF-based electronics. Further study along these lines is warranted.

■ ASSOCIATED CONTENT

Supporting Information

The Supporting Information is available free of charge on the ACS Publications website at DOI: 10.1021/jacs.7b11888.

Details regarding the preparation of PDI films via vapor deposition and their structural characterization using AFM, GIWAXS, and steady-state optical probes; additional time-resolved emission and TA spectra not highlighted in the main text; discussion of photoinduced heating signatures in TA spectra; description of the kinetic model used to extract SF rates from time-resolved data; methods used to calculate PDI singlet and triplet exciton energies from a Holstein-type Hamiltonian and PDI SF rate from Marcus theory (PDF)

■ AUTHOR INFORMATION

Corresponding Author

*roberts@cm.utexas.edu

ORCID

Aaron K. Le: 0000-0003-2247-3901
Jon A. Bender: 0000-0003-1713-1480
Dylan H. Arias: 0000-0003-2358-6967
Daniel E. Cotton: 0000-0002-5170-7108
Justin C. Johnson: 0000-0002-8874-6637
Sean T. Roberts: 0000-0002-3322-3687

Author Contributions

§AKL and JAB contributed equally to this manuscript.

Notes

The authors declare no competing financial interest.

■ ACKNOWLEDGMENTS

Work performed at the University of Texas at Austin was supported by the Robert A. Welch Foundation (Grant F-1885) and the National Science Foundation (CAREER Award: CHE-1654404). D.H.A. and J.C.J. acknowledge support from the U.S. Department of Energy, Office of Basic Energy Sciences, Division of Chemical Sciences, Biosciences, and Geosciences, through Contract No. DE-AC36-08GO28308 with NREL for streak camera collection of time-resolved emission data. The authors also acknowledge Dr. Nicholas Hestand and Dr. Frank Spano for providing aid with regards to the calculation of PDI film electronic structure, as well as Dr. Nicolas Renaud and Dr. Ferdinand Grozema for providing the results of calculations published in ref 56. Computational resources in support of this work were provided by the Texas Advanced Computing Center (TACC) at The University of Texas at Austin. The authors would also like to acknowledge Dr. Raluca Gearba of the Texas Materials Institute at the University of Texas at Austin for aid in thin film preparation and characterization.

■ REFERENCES

(1) Smith, M. B.; Michl, J. *Chem. Rev.* **2010**, *110* (11), 6891−6936.
(2) Smith, M. B.; Michl, J. *Annu. Rev. Phys. Chem.* **2013**, *64*, 361−386.
(3) Singh, S.; Jones, W. J.; Siebrand, W.; Stoicheff, B. P.; Schneider, W. G. *J. Chem. Phys.* **1965**, *42* (1), 330−342.
(4) Shockley, W.; Queisser, H. J. *J. Appl. Phys.* **1961**, *32* (3), 510−519.
(5) Hanna, M. C.; Nozik, A. J. *J. Appl. Phys.* **2006**, *100*, 74510.
(6) Tayebjee, M. J. Y.; Gray-Weale, A. A.; Schmidt, T. W. *J. Phys. Chem. Lett.* **2012**, *3*, 2749−2754.
(7) Tayebjee, M. J. Y.; McCamey, D. R.; Schmidt, T. W. *J. Phys. Chem. Lett.* **2015**, *6* (12), 2367−2378.
(8) Musser, A. J.; Maiuri, M.; Brida, D.; Cerullo, G.; Friend, R. H.; Clark, J. *J. Am. Chem. Soc.* **2015**, *137* (15), 5130−5139.
(9) Wang, C.; Tauber, M. J. *J. Am. Chem. Soc.* **2010**, *132* (40), 13988−13991.
(10) Zhang, Y.; Forrest, S. R. *Phys. Rev. Lett.* **2012**, *108* (26), 267404.
(11) Nienhaus, L.; Wu, M.; Geva, N.; Shepherd, J. J.; Wilson, M. W. B.; Bulović, V.; Van Voorhis, T.; Baldo, M. A.; Bawendi, M. G. *ACS Nano* **2017**, *11* (8), 7848−7857.
(12) Wu, M.; Congreve, D. N.; Wilson, M. W. B.; Jean, J.; Geva, N.; Welborn, M.; Van Voorhis, T.; Bulović, V.; Bawendi, M. G.; Baldo, M. A. *Nat. Photonics* **2015**, *10* (1), 31−34.
(13) Mongin, C.; Garakyaraghi, S.; Razgoniaeva, N.; Zamkov, M.; Castellano, F. N. *Science* **2016**, *351*, 369−372.
(14) Huang, Z.; Li, X.; Mahboub, M.; Hanson, K. M.; Nichols, V. M.; Le, H.; Tang, M. L.; Bardeen, C. J. *Nano Lett.* **2015**, *15* (8), 5552−5557.
(15) Huang, Z.; Tang, M. L. *J. Am. Chem. Soc.* **2017**, *139* (28), 9412−9418.
(16) Johnson, J. C.; Nozik, A. J.; Michl, J. *J. Am. Chem. Soc.* **2010**, *132* (46), 16302−16303.
(17) Schrauben, J. N.; Ryerson, J. L.; Michl, J.; Johnson, J. C. *J. Am. Chem. Soc.* **2014**, *136* (20), 7363−7373.
(18) Hartnett, P. E.; Margulies, E. A.; Mauck, C. M.; Miller, S. A.; Wu, Y.; Wu, Y.-L.; Marks, T. J.; Wasielewski, M. R. *J. Phys. Chem. B* **2016**, *120* (7), 1357−1366.
(19) Lanzani, G.; Cerullo, G.; Zavelani-Rossi, M.; Silvestri, S. D.; Comoretto, D.; Musso, G.; Dellepiane, G. *Phys. Rev. Lett.* **2001**, *87* (18), 187402.
(20) Musser, A. J.; Al-Hashimi, M.; Maiuri, M.; Brida, D.; Heeney, M.; Cerullo, G.; Friend, R. H.; Clark, J. *J. Am. Chem. Soc.* **2013**, *135* (34), 12747−12754.
(21) Tamai, Y.; Ohkita, H.; Benten, H.; Ito, S. *J. Phys. Chem. C* **2013**, *117* (20), 10277−10284.
(22) Geacintov, N.; Pope, M.; Vogel, F. *Phys. Rev. Lett.* **1969**, *22* (12), 593−596.
(23) Swenberg, C. E.; Stacy, W. T. *Chem. Phys. Lett.* **1968**, *2* (5), 327−328.
(24) Merrifield, R. E.; Avakian, P.; Groff, R. P. *Chem. Phys. Lett.* **1969**, *3* (6), 386−388.
(25) Burdett, J. J.; Gosztola, D.; Bardeen, C. J. *J. Chem. Phys.* **2011**, *135*, 214508.
(26) Piland, G. B.; Bardeen, C. J. *J. Phys. Chem. Lett.* **2015**, *6* (10), 1841−1846.
(27) Wilson, M. W. B.; Rao, A.; Clark, J.; Kumar, R. S. S.; Brida, D.; Cerullo, G.; Friend, R. H. *J. Am. Chem. Soc.* **2011**, *133* (31), 11830−11833.
(28) Busby, E.; Berkelbach, T. C.; Kumar, B.; Chernikov, A.; Zhong, Y.; Hlaing, H.; Zhu, X. Y.; Heinz, T. F.; Hybertsen, M. S.; Sfeir, M. Y.; Reichman, D. R.; Nuckolls, C.; Yaffe, O. *J. Am. Chem. Soc.* **2014**, *136* (30), 10654−10660.
(29) Piland, G. B.; Burdett, J. J.; Kurunthu, D.; Bardeen, C. J. *J. Phys. Chem. C* **2013**, *117*, 1224−1236.
(30) Roberts, S. T.; McAnally, R. E.; Mastron, J. N.; Webber, D. H.; Whited, M. T.; Brutchey, R. L.; Thompson, M. E.; Bradforth, S. E. *J. Am. Chem. Soc.* **2012**, *134* (14), 6388−6400.
(31) Arias, D. H.; Ryerson, J. L.; Cook, J. D.; Damrauer, N. H.; Johnson, J. C. *Chem. Sci.* **2016**, *7* (2), 1185−1191.
(32) Sanders, S. N.; Kumarasamy, E.; Pun, A. B.; Trinh, M. T.; Choi, B.; Xia, J.; Taffet, E. J.; Low, J. Z.; Miller, J. R.; Roy, X.; Zhu, X.-Y.; Steigerwald, M. L.; Sfeir, M. Y.; Campos, L. M. *J. Am. Chem. Soc.* **2015**, *137* (28), 8965−8972.
(33) Korovina, N. V.; Das, S.; Nett, Z.; Feng, X.; Joy, J.; Haiges, R.; Krylov, A. I.; Bradforth, S. E.; Thompson, M. E. *J. Am. Chem. Soc.* **2016**, *138* (2), 617−627.

DOI: 10.1021/jacs.7b11888
J. Am. Chem. Soc. 2018, 140, 814−826

(34) Zirzlmeier, J.; Lehnherr, D.; Coto, P. B.; Chernick, E. T.; Casillas, R.; Basel, B. S.; Thoss, M.; Tykwinski, R. R.; Guldi, D. M. *Proc. Natl. Acad. Sci. U. S. A.* **2015**, *112* (17), 5325−5330.
(35) Kumarasamy, E.; Sanders, S. N.; Tayebjee, M. J. Y.; Asadpoordarvish, A.; Hele, T. J. H.; Fuemmeler, E. G.; Pun, A. B.; Yablon, L. M.; Low, J. Z.; Paley, D. W.; Dean, J. C.; Choi, B.; Scholes, G. D.; Steigerwald, M. L.; Ananth, N.; McCamey, D. R.; Sfeir, M. Y.; Campos, L. M. *J. Am. Chem. Soc.* **2017**, *139* (36), 12488−12494.
(36) Cook, J. D.; Carey, T. J.; Damrauer, N. H. *J. Phys. Chem. A* **2016**, *120* (26), 4473−4481.
(37) Liu, H.; Wang, R.; Shen, L.; Xu, Y.; Xiao, M.; Zhang, C.; Li, X. *Org. Lett.* **2017**, *19* (3), 580−583.
(38) Sanders, S. N.; Kumarasamy, E.; Pun, A. B.; Steigerwald, M. L.; Sfeir, M. Y.; Campos, L. M. *Chem.* **2016**, *1* (3), 505−511.
(39) Congreve, D. N.; Lee, J.; Thompson, N. J.; Hontz, E.; Yost, S. R.; Reusswig, P. D.; Bahlke, M. E.; Reineke, S.; Voorhis, T. V.; Baldo, M. A. *Science* **2013**, *340*, 334−337.
(40) Pazos-Outón, L. M.; Lee, J. M.; Futscher, M. H.; Kirch, A.; Tabachnyk, M.; Friend, R. H.; Ehrler, B. *ACS Energy Lett.* **2017**, *2* (2), 476−480.
(41) Tabachnyk, M.; Ehrler, B.; Bayliss, S.; Friend, R. H.; Greenham, N. C. *Appl. Phys. Lett.* **2013**, *103*, 153302−153302.
(42) Kaur, I.; Jia, W.; Kopreski, R. P.; Selvarasah, S.; Dokmeci, M. R.; Pramanik, C.; McGruer, N. E.; Miller, G. P. *J. Am. Chem. Soc.* **2008**, *130* (48), 16274−16286.
(43) Wurthner, F. *Chem. Commun.* **2004**, *0*, 1564−1579.
(44) Ford, W. E.; Kamat, P. V. *J. Phys. Chem.* **1987**, *91*, 6373−6380.
(45) Lohmannsroben, H. G.; Langhals, H. *Appl. Phys. B: Photophys. Laser Chem.* **1989**, *48*, 449−452.
(46) Eaton, S. W.; Shoer, L. E.; Karlen, S. D.; Dyar, S. M.; Margulies, E. A.; Veldkamp, B. S.; Ramanan, C.; Hartzler, D. A.; Savikhin, S.; Marks, T. J.; Wasielewski, M. R. *J. Am. Chem. Soc.* **2013**, *135* (39), 14701−14712.
(47) Nakazono, S.; Easwaramoorthi, S.; Kim, D.; Shinokubo, H.; Osuka, A. *Org. Lett.* **2009**, *11* (23), 5426−5429.
(48) Langhals, H.; Karolin, J.; Johansson, L. B.-A. *J. Chem. Soc., Faraday Trans.* **1998**, *94* (19), 2919−2922.
(49) Huang, C.; Barlow, S.; Marder, S. R. *J. Org. Chem.* **2011**, *76* (8), 2386−2407.
(50) Burgdorff, C.; Kircher, T.; Löhmannsröben, H.-G. *Spectrochim. Acta. A. Mol. Biomol. Spectrosc.* **1988**, *44A* (11), 1137−1141.
(51) Burgdorff, C.; Ehrhardt, S.; Loehmannsroeben, H. G. *J. Phys. Chem.* **1991**, *95* (11), 4246−4249.
(52) Bruzek, M. J.; Anthony, J. E. *Org. Lett.* **2014**, *16* (13), 3608−3610.
(53) *High Performance Pigments*; Faulkner, E. B., Schwartz, R. J., Eds.; Wiley-VCH: Weinheim, 2009.
(54) Herbst, W.; Hunger, K.; Wilker, G. *Industrial Organic Pigments: Production, Properties, Applications*, 3rd compl. rev. ed.; Wiley-VCH: Weinheim, 2004.
(55) Fukuzumi, S.; Ohkubo, K.; Ortiz, J.; Gutiérrez, A. M.; Fernández-Lázaro, F.; Sastre-Santos, A. *J. Phys. Chem. A* **2008**, *112* (43), 10744−10752.
(56) Mirjani, F.; Renaud, N.; Gorczak, N.; Grozema, F. C. *J. Phys. Chem. C* **2014**, *118* (26), 14192−14199.
(57) Renaud, N.; Sherratt, P. A.; Ratner, M. A. *J. Phys. Chem. Lett.* **2013**, *4* (7), 1065−1069.
(58) Renaud, N.; Grozema, F. C. *J. Phys. Chem. Lett.* **2015**, *6* (3), 360−365.
(59) Klebe, G.; Graser, F.; Hädicke, E.; Berndt, J. *Acta Crystallogr., Sect. B: Struct. Sci.* **1989**, *45* (1), 69−77.
(60) Briseno, A. L.; Mannsfeld, S. C. B.; Reese, C.; Hancock, J. M.; Xiong, Y.; Jenekhe, S. A.; Bao, Z.; Xia, Y. *Nano Lett.* **2007**, *7* (9), 2847−2853.
(61) Hadicke, E.; Graser, F. *Acta Crystallogr., Sect. C: Cryst. Struct. Commun.* **1986**, *C42*, 189−195.
(62) Hadicke, E.; Graser, F. *Acta Crystallogr., Sect. C: Cryst. Struct. Commun.* **1986**, *C42*, 195−198.
(63) Miller, C. E.; Wasielewski, M. R.; Schatz, G. C. *J. Phys. Chem. C* **2017**, *121* (19), 10345−10350.
(64) Le, A. K.; Bender, J. A.; Roberts, S. T. *J. Phys. Chem. Lett.* **2016**, *7* (23), 4922−4928.
(65) Nečas, D.; Klapetek, P. *Cent. Eur. J. Phys.* **2012**, *10* (1), 181−188.
(66) Kasha, M.; Rawls, H. R.; El-Bayoumi, M. A. *Pure Appl. Chem.* **1965**, *11*, 371−392.
(67) Kazmaier, P. M.; Hoffmann, R. A. *J. Am. Chem. Soc.* **1994**, *116* (21), 9684−9691.
(68) Hestand, N. J.; Spano, F. C. *J. Chem. Phys.* **2015**, *143* (24), 244707.
(69) Hestand, N. J.; Spano, F. C. *Acc. Chem. Res.* **2017**, *50* (2), 341−350.
(70) Yamagata, H.; Maxwell, D. S.; Fan, J.; Kittilstved, K. R.; Briseno, A. L.; Barnes, M. D.; Spano, F. C. *J. Phys. Chem. C* **2014**, *118* (49), 28842−28854.
(71) Paci, I.; Johnson, J. C.; Chen, X.; Rana, G.; Popovic, D.; David, D. E.; Nozik, A. J.; Ratner, M. A.; Michl, J. *J. Am. Chem. Soc.* **2006**, *128*, 16546−16553.
(72) Johnson, J. C.; Akdag, A.; Zamadar, M.; Chen, X.; Schwerin, A. F.; Paci, I.; Smith, M. B.; Havlas, Z.; Miller, J. R.; Ratner, M. A.; Nozik, A. J.; Michl, J. *J. Phys. Chem. B* **2013**, *117* (16), 4680−4695.
(73) Margulies, E. A.; Miller, C. E.; Wu, Y.; Ma, L.; Schatz, G. C.; Young, R. M.; Wasielewski, M. R. *Nat. Chem.* **2016**, *8* (12), 1120−1125.
(74) Berkelbach, T. C.; Hybertsen, M. S.; Reichman, D. R. *J. Chem. Phys.* **2013**, *138*, 114102.
(75) Berkelbach, T. C.; Hybertsen, M. S.; Reichman, D. R. *J. Chem. Phys.* **2013**, *138*, 114103.
(76) Wiederrecht, G. P.; Svec, W. A.; Wasielewski, M. R.; Galili, T.; Levanon, H. *J. Am. Chem. Soc.* **2000**, *122* (40), 9715−9722.
(77) Whited, M. T.; Patel, N. M.; Roberts, S. T.; Allen, K.; Djurovich, P. I.; Bradforth, S. E.; Thompson, M. E. *Chem. Commun.* **2012**, *48* (2), 284−286.
(78) Bartynski, A. N.; Gruber, M.; Das, S.; Rangan, S.; Mollinger, S.; Trinh, C.; Bradforth, S. E.; Vandewal, K.; Salleo, A.; Bartynski, R. A.; Bruetting, W.; Thompson, M. E. *J. Am. Chem. Soc.* **2015**, *137* (16), 5397−5405.
(79) Vauthey, E. *ChemPhysChem* **2012**, *13* (8), 2001−2011.
(80) Marcon, R. O.; Brochsztain, S. *J. Phys. Chem. A* **2009**, *113* (9), 1747−1752.
(81) Gosztola, D.; Niemczyk, M. P.; Svec, W.; Lukas, A. S.; Wasielewski, M. R. *J. Phys. Chem. A* **2000**, *104* (28), 6545−6551.
(82) Ford, W. E.; Hiratsuka, H.; Kamat, P. V. *J. Phys. Chem.* **1989**, *93* (18), 6692−6696.
(83) Brown, K. E.; Salamant, W. A.; Shoer, L. E.; Young, R. M.; Wasielewski, M. R. *J. Phys. Chem. Lett.* **2014**, *5*, 2588−2593.
(84) Cook, R. E.; Phelan, B. T.; Kamire, R. J.; Majewski, M. B.; Young, R. M.; Wasielewski, M. R. *J. Phys. Chem. A* **2017**, *121* (8), 1607−1615.
(85) Lindquist, R. J.; Lefler, K. M.; Brown, K. E.; Dyar, S. M.; Margulies, E. A.; Young, R. M.; Wasielewski, M. R. *J. Am. Chem. Soc.* **2014**, *136* (42), 14912−14923.
(86) Margulies, E. A.; Logsdon, J. L.; Miller, C. E.; Ma, L.; Simonoff, E.; Young, R. M.; Schatz, G. C.; Wasielewski, M. R. *J. Am. Chem. Soc.* **2017**, *139* (2), 663−671.
(87) Margulies, E. A.; Shoer, L. E.; Eaton, S. W.; Wasielewski, M. R. *Phys. Chem. Chem. Phys.* **2014**, *16* (43), 23735−23742.
(88) Caplins, B. W.; Mullenbach, T. K.; Holmes, R. J.; Blank, D. A. *Phys. Chem. Chem. Phys.* **2016**, *18* (16), 11454−11459.
(89) Dutton, G. J.; Robey, S. W. *J. Phys. Chem. C* **2012**, *116* (36), 19173−19181.
(90) Roberts, S. T.; Schlenker, C. W.; Barlier, V.; McAnally, R. E.; Zhang, Y.; Mastron, J. N.; Thompson, M. E.; Bradforth, S. E. *J. Phys. Chem. Lett.* **2011**, *2*, 48−54.
(91) Yu, Z.; Wu, Y.; Peng, Q.; Sun, C.; Chen, J.; Yao, J.; Fu, H. *Chem. - Eur. J.* **2016**, *22* (14), 4717−4722.

DOI: 10.1021/jacs.7b11888
J. Am. Chem. Soc. 2018, 140, 814−826

(92) Rao, A.; Wilson, M. W. B.; Albert-Seifried, S.; Pietro, R. D.; Friend, R. H. *Phys. Rev. B: Condens. Matter Mater. Phys.* **2011**, *84*, 195411−195411.
(93) Albert-Seifried, S.; Friend, R. H. *Appl. Phys. Lett.* **2011**, *98* (22), 223304.
(94) Müller, A. M.; Avlasevich, Y. A.; Schoeller, W. W.; Müllen, K.; Bardeen, C. J. *J. Am. Chem. Soc.* **2007**, *129*, 14240−14250.
(95) Yong, C. K.; Musser, A. J.; Bayliss, S. L.; Lukman, S.; Tamura, H.; Bubnova, O.; Hallani, R. K.; Meneau, A.; Resel, R.; Maruyama, M.; Hotta, S.; Herz, L. M.; Beljonne, D.; Anthony, J. E.; Clark, J.; Sirringhaus, H. *Nat. Commun.* **2017**, *8*, 15953.
(96) Pensack, R. D.; Ostroumov, E. E.; Tilley, A. J.; Mazza, S.; Grieco, C.; Thorley, K. J.; Asbury, J. B.; Seferos, D. S.; Anthony, J. E.; Scholes, G. D. *J. Phys. Chem. Lett.* **2016**, *7* (13), 2370−2375.
(97) Breen, I.; Tempelaar, R.; Bizimana, L. A.; Kloss, B.; Reichman, D. R.; Turner, D. B. *J. Am. Chem. Soc.* **2017**, *139* (34), 11745−11751.
(98) Shushin, A. I. *Chem. Phys. Lett.* **2017**, *678*, 283−288.
(99) Chan, W.-L.; Ligges, M.; Jailaubekov, A.; Kaake, L.; Miaja-Avila, L.; Zhu, X.-Y. *Science* **2011**, *334* (6062), 1541−1545.
(100) Ramanan, C.; Smeigh, A. L.; Anthony, J. E.; Marks, T. J.; Wasielewski, M. R. *J. Am. Chem. Soc.* **2012**, *134* (1), 386−397.
(101) Pensack, R. D.; Tilley, A. J.; Parkin, S. R.; Lee, T. S.; Payne, M. M.; Gao, D.; Jahnke, A. A.; Oblinsky, D. G.; Li, P.-F.; Anthony, J. E.; Seferos, D. S.; Scholes, G. D. *J. Am. Chem. Soc.* **2015**, *137* (21), 6790−6803.
(102) Ern, V.; Saint-Clair, J. L.; Schott, M.; Delacote, G. *Chem. Phys. Lett.* **1971**, *10* (3), 287−290.
(103) Arnold, S.; Wotherspoon, N. *Rev. Sci. Instrum.* **1976**, *47* (6), 751−753.
(104) Delannoy, P.; Schott, M. *Phys. Status Solidi B* **1975**, *70* (1), 119−131.
(105) Peter, L.; Vaubel, G. *Phys. Status Solidi B* **1971**, *48* (2), 587−590.
(106) Vaubel, G.; Baessler, H. *Phys. Status Solidi B* **1970**, *37* (1), K31−K34.
(107) Burdett, J. J.; Müller, A. M.; Gosztola, D.; Bardeen, C. J. *J. Chem. Phys.* **2010**, *133*, 144506.
(108) Wan, Y.; Guo, Z.; Zhu, T.; Yan, S.; Johnson, J.; Huang, L. *Nat. Chem.* **2015**, *7*, 785−792.
(109) Najafov, H.; Lee, B.; Zhou, Q.; Feldman, L. C.; Podzorov, V. *Nat. Mater.* **2010**, *9*, 938−943.
(110) Irkhin, P.; Biaggio, I. *Phys. Rev. Lett.* **2011**, *107* (1), 017402.
(111) Akselrod, G. M.; Deotare, P. B.; Thompson, N. J.; Lee, J.; Tisdale, W. A.; Baldo, M. A.; Menon, V. M.; Bulović, V. *Nat. Commun.* **2014**, *5*, 3646.
(112) Kolomeisky, A. B.; Feng, X.; Krylov, A. I. *J. Phys. Chem. C* **2014**, *118* (10), 5188−5195.
(113) Feng, X.; Krylov, A. I. *Phys. Chem. Chem. Phys.* **2016**, *18* (11), 7751−7761.
(114) Quarti, C.; Fazzi, D.; Del Zoppo, M. *Phys. Chem. Chem. Phys.* **2011**, *13* (41), 18615.

DOI: 10.1021/jacs.7b11888
J. Am. Chem. Soc. 2018, 140, 814−826